J. Fluid Mech. (2018), *vol.* 846, *pp.* 1088–1113.
doi:10.1017/jfm.2018.262

Modelling levitated 2-lobed droplets in rotation using Cassinian oval curves

Haruki Ishikawa[1,†] **and Katsuhiro Nishinari**[2]

[1]Department of Aeronautics and Astronautics, School of Engineering, The University of Tokyo, 7-3-1, Hongo, Bunkyo-ku, Tokyo 113-8656, Japan

[2]Research Center for Advanced Science and Technology, The University of Tokyo, 4-6-1, Komaba, Meguro-ku, Tokyo 153-8904, Japan

(Received 9 June 2017; revised 8 March 2018; accepted 22 March 2018; first published online 15 May 2018)

A simple model of rotating 2-lobed droplets is proposed by setting the outline shape of the droplet to the Cassinian oval, a mathematical curve that closely resembles in shape. By deriving the governing equation of the proposed model and obtaining its stationary solutions, the relationship between the angular velocity of rotation and the maximum deformation length is explicitly and precisely calculated. The linear stability analysis is performed for the stationary solutions, and it is demonstrated that the stability of the solutions depends only on the ratio of the deformation length to the radius of the central cross-section of the droplet, which is independent of the physical properties of the droplet. Via comparison with an experimental study, it is observed that the calculated result is consistent with the deformation behaviour of actual 2-lobed droplets in the range where the stationary solution of the proposed model is linearly stable. Therefore, the proposed model is a suitable model for reproducing the steady deformation behaviour of 2-lobed droplets in a wide range of viscosities, surface tensions, densities and initial radii of the droplet, and especially if the viscosity of the droplet is low, the entire process of deformation of the 2-lobed droplet, including the unsteady breakup process, can be very well reproduced by the proposed model.

Key words: drops, drops and bubbles

1. Introduction

The dynamics of droplets is one of the most interesting topics in fluid mechanics owing to its nonlinearity and variety of behaviour (Frohn & Roth 2000). Over more than a century, a large number of studies have been performed to solve the dynamics of droplets, e.g. a study on the eigenfrequency of the capillary oscillations of spherical droplets (Rayleigh 1879) and studies on the self-gravitating shapes of rotating gas planets and their shape retainability (reviewed in Chandrasekhar (1967)). In particular, the process where a droplet in rotation deforms until it breaks up has been actively studied. Recent theoretical studies have originated from Poincaré's study, in which the existence of equilibrium shapes that are not axisymmetric with respect to the rotation axis, which is classified into 2-lobed droplets in recent studies, was

† Email address for correspondence: ishikawa@jamology.rcast.u-tokyo.ac.jp

demonstrated (Poincaré 1885). Chandrasekhar was the first to theoretically consider the stability of rotating droplets (Chandrasekhar 1965). In 1980, Brown and Scriven extensively investigated the equilibrium shapes via expansions in finite element analysis, classified them into several families according to their rotational symmetry and discussed the stability of each family (Brown & Scriven 1980). In the analysis of the deformation of rotating droplets, numerically solving the shape-determining equation by combining the division of the interface with finite elements and by Galerkin expansion is one of the most useful techniques, and deforming behaviours of 2-lobed droplets that were not observed in the study (Brown & Scriven 1980) have been discovered. For instance, 2-lobed sectional shapes with a liquid filament have also been observed (Benner, Basaran & Scriven 1991) and oscillations of the droplet interface on the section perpendicular to the axis of rotation have been analysed with high accuracy (Patzek *et al.* 1995). In recent decades, along with improvements in techniques for levitating droplets (reviewed in Brandt (1989)), the processes by which rotating droplets significantly deform and break up have been collectively regarded as an important subject in many fields owing to their applicability to centrifuging fluids, splaying liquids and containerless chemical reactions. Therefore, numerous experimental studies have been conducted in simulated microgravity environments; e.g. in microgravity environments in low Earth orbits (Wang *et al.* 1986), in electrostatic fields (Rhim *et al.* 1985; Tanaka *et al.* 2013), magnetic fields (Beaugnon & Tournier 1991; Beaugnon *et al.* 2001) or ultrasonic fields (Trinh 1985) in laboratories. In such experimental studies, droplets in the 2-lobed family have been confirmed and their breakup has been observed (e.g. Rhim, Chung & Elleman 1990, Wang *et al.* 1994). Studies on the dynamic and unsteady behaviour of droplets have also been conducted. For instance, a multi-lobed droplet in rotation was stabilised by generating a surface wave travelling around its equator, and the process of transition from the stably rotating pentagon shape to the 2-lobed peanut shape was experimentally observed (Hill & Eaves 2008). In other studies, the process of binary droplet collision and internal mixing, which is considered to progress while assuming a shape similar to that immediately before the breakup of a 2-lobed droplet under certain conditions of coalescence, has been studied experimentally and numerically (Qian & Law 1997; Sun *et al.* 2015). Moreover, following further improvements in techniques for levitating droplets, precise control of the positions of levitated droplets and manipulation of the droplets were realised by appropriately varying the ultrasonic levitation field, and coalescence of droplets with a wider range of Weber numbers has become possible (Foresti *et al.* 2013). As demonstrated in the above studies, the entire process of large deformation and breakup of 2-lobed droplets is also of fundamental importance to various engineering processes such as manipulating the size and shape of ink droplets in ink-jet printing (van der Bos *et al.* 2014) and non-contact measurement of viscosity and surface tension of various materials (Ohsaka *et al.* 2002; Tanaka *et al.* 2013).

Techniques of levitating various materials have been applied in many fields outside fluid mechanics, because such non-contact handling of levitated materials enables non-contact heating, melting and solidification of the materials. In Baldwin, Butler & Hill (2015), the authors levitated droplets of molten wax, deformed the droplets into an oblate ellipsoid or 2-lobed ‘dumbbell-like’ shape by applying external forces and solidified these droplets in stable rotation, in order to artificially reproduce splash-form tektites with high accuracy (Baldwin *et al.* 2015). Splash-form tektites, which are glassy stones formed from molten rock ejected from asteroid impacts, are observed in shapes of revolution including 2-lobed ‘dumbbell’ shapes, and artificial tektites

with these shapes made of various materials have been manufactured in laboratories (Elkins-Tanton *et al.* 2003). As demonstrated in the above studies, many such tektites are consistent with the numerical solution of equilibrium shape (Brown & Scriven 1980); however, largely elongated 2-lobed tektites with a small circumference in the central cross-section and 'tear-drop' shaped tektites have been observed. It is considered that these tektites have solidified in the state where the rotational angular momentum exceeds the boundary of the stability and the process of pinch off is progressing, and these facts has been confirmed by numerical calculations (Butler *et al.* 2011). As demonstrated in the aforementioned examples, determining the shape of levitated droplets in rotation is a significant topic in theoretical and experimental research, and is expected to be widely applied in various fields.

From the viewpoint of physics, when an axial symmetry fluid is driven by an external force whose direction is along the axisymmetrical axis of the flow, the locally formed liquid thread breaks up owing to the Plateau–Rayleigh instability and droplets separate from the flow (Eggers 1997). As the deformation of the 2-lobed droplet in rotation is mainly driven by the centrifugal force whose direction is parallel to the axisymmetrical axis of the droplet shape at the moment the breakup of an extended 2-lobed drop occurs, it is considered that the pinch off of the neck region occurs owing to the same instability. Here, in this context, the axisymmetrical axis of the shape is the longitudinal axis of the 2-lobed ('dumbbell-like' shaped) droplets in rotation, not the axis of rotational angular velocity. The progress of deformation is primarily affected by the interaction among three forces: the force of inertia, centrifugal force and surface tension proportional to the mean curvature of the surface of the droplet. Accordingly, to evaluate the deformation and breakup of a rotating 2-lobed droplet, the entire shape of the droplet should be precisely modelled for every state of deformation of the 2-lobed droplet until the radius of the central cross-section decreases to 0 and the droplet breaks up. There have been several previous studies in which the process of deformation of the 2-lobed droplet in rotation was divided into several stages based on the radius of the central cross-section and the shape of each stage was modelled to quantitatively evaluate the deformation (e.g. Aussillous & Quéré 2004); however, there has not been any study that has proposed a single model to describe almost the entire process of deformation of rotating 2-lobed droplets.

In this study, we propose a simple model of rotating 2-lobed droplets to evaluate almost the entire process by which a 2-lobed droplet is stretched until it breaks up. The proposed model, which is called 'the Cassinian droplet model' in this paper, is developed by setting the contour shape of the droplet equal to the Cassinian oval, a series of mathematical curves that closely resemble 2-lobed droplets in shape. We derive the governing equations describing the deformation of the Cassinian droplet in rotation and, by obtaining the stationary solution of the governing equation, we explicitly calculate the relationship between the angular velocity of rotation and the maximum deformation length. Furthermore, we conduct a linear stability analysis of the stationary solution and demonstrate that the condition of linear stability depends only on the ratio of the maximum deformation length to the radius of the central cross-section of the 2-lobed droplet, regardless of its physical properties, i.e. viscosity, surface tension, density and volume of the droplet. Further, it is observed that the relationship between the angular velocity of rotation and the maximum deformation length originally computed by Brown and Scriven in 1980 is closely reproduced by the linearly stable stationary solutions of the proposed model. Moreover, as a result of a comparison with an experimental study (Tanaka *et al.* 2013), we found that there is excellent agreement between the set of linearly stable stationary solutions of the

proposed model and the deformation of experimentally stretched 2-lobed droplets for a wide range of physical properties of the droplet. Finally, by deriving the exact solution of the governing equations of the deformation of the Cassinian droplet under the limit of extremely low viscosity, it is observed that the process by which an extremely low-viscosity 2-lobed droplet breaks up is very well reproduced by the proposed model. Therefore, it is confirmed that the proposed 'Cassinian droplet model' very accurately reproduces the entire process by which an extremely low-viscosity 2-lobed droplet in rotation deforms until breakup.

The shape of a rotating 2-lobed droplet is reproduced by only one deformation variable and one fixed parameter by utilising the proposed 'Cassinian droplet' model due to volume preservation, while the true shape obtained by solving a shape-determining equation in the boundary element method is determined by infinitely many parameters. The angular velocity of rotation, the maximum deformation length, the radius of the central cross-section and other characteristic quantities of deformation are also expressed as a function of the variable with a fixed parameter. Then, we can understand intuitively the progress of deformation of a rotating 2-lobed droplet by executing differentiation of the shape of the Cassinian droplet with the shape-determining variable.

A major advantage of proposing 'Cassinian droplet model' is that we can analyse precisely the process by which a 2-lobed droplet unsteady deforms until it breaks up. When an actual extremely low-viscosity droplet breaks up, the radius of the central cross-section rapidly decreases and a singular shape, a very sharp conical interface, appears at the vicinity of the midpoint, and the breakup limit of the Cassinian droplet also has a very similar shape. Numerical calculation of deformation of rotating levitated droplets by utilising the boundary element method is highly compatible with calculations of equilibrium shape of 2-lobed droplets in rotation. However, in the calculation for the deformation of a droplet whose shape losses equilibrium and that largely elongates until breakup, it has been reported that numerical calculation stops before pinch off of the central cross-section occurs due to failure to re-mesh its boundary (Butler *et al.* 2011; Baldwin *et al.* 2015). By contrast, by utilising the proposed 'Cassinian droplet model', unstable breaking-up behaviour is reproduced in high accuracy with less calculation cost, and such numerical failures do not occur even at the moment of breakup. It is because the shape of the 2-lobed droplet is generated directly from the shape-determining function (the Cassinian oval curve) that precisely reproduces the shape until the moment that the droplet breaks up. Further, if the droplet consists of extremely low-viscosity liquid, an exact solution of the stress-balance equation of the Cassinian droplet is explicitly obtained, and the time for breakup required from the stability limit of the steady-state solution can be explicitly calculated.

As demonstrated in the following text, the proposed 'Cassinian droplet model' has been able to reproduce almost the entire process of large deformation and breakup of a rotating 2-lobed droplet in very precise approximation. We show that the Cassinian oval curve does simulate actually shapes of levitated 2-lobed droplets in rotation very well, however simulating shape is not the goal of this study but the process of the following objective. By using the proposed model, various quantities of breaking-up behaviours of 2-lobed droplets can be not only numerically but also theoretically calculated under the assumption of the model. An exact solution for obtaining the time required for breakup is just an example. From above facts, we consider that this study leads to the proposal of a new analytical method that can be utilised to solve almost the entire process by which a rotating 2-lobed droplet largely deforms until it breaks up in high accuracy and that is particularly compatible with the process of breakup.

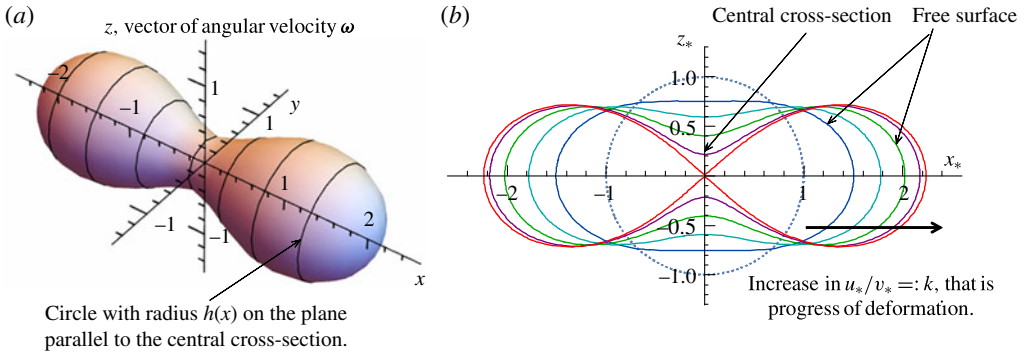

FIGURE 1. (Colour online) (*a*) Schematic of a 2-lobed droplet and the rotational Cartesian frame fixed to the rotating droplet. The origin is located at the centre of gravity of the droplet, the z axis and the x axis are fixed to the vector of angular velocity $\boldsymbol{\omega}$ and the axisymmetrical axis of the droplet shape, respectively. The cross-sectional radius at the position x is $h(x)$. (*b*) Side view of Cassinian droplets in the rotating frame drawn using (2.9) and the equation of volume conservation. The parameter A is 0.8210, which is the same value as A_{opt} determined in § 3. The solid lines are a series of Cassinian droplets for $u_*/v_* := R_{Max*}/H_{mid*} = 2,\ 3,\ 5,\ 10$ and 150 (blue, light blue, green, purple, red lines, respectively). The outward arrow at the bottom right of the figure shows the increase in k, that is, the progress of deformation. The broken line indicates a spherical drop with the same volume.

2. Model development

In the present study, we focus on the 2-lobed branch of the deformation of levitated droplets in rotation, the branch on which angular velocity of rotation decreases as the deformation length increases. In this section, we develop a simple model describing the deforming behaviour of 2-lobed droplets in rotation and derive the governing equations of the progress of deformation, the stress-balance equation in the longitudinal direction of the 2-lobed droplet and the equation of angular momentum conservation.

We consider a levitated 2-lobed fluid drop rotating around a fixed axis that passes through its centre of gravity (figure 1*a*). As the 2-lobed droplet has an axisymmetrical axis of the droplet shape that is perpendicular to the angular velocity vector, the droplet surface can be expressed as

$$\boldsymbol{s}(x, \theta) = (x, h(x)\cos\theta,\ \ h(x)\sin\theta)^{\mathrm{T}} (-R_{Max} \leqslant x \leqslant R_{Max},\ 0 \leqslant \theta \leqslant 2\pi), \tag{2.1}$$

in Cartesian coordinates where the centre of gravity of the droplet is at the origin, the axisymmetrical axis of the droplet shape is along the x-axis and the direction of the angular velocity vector is along the z-axis. The y-axis is set by following the right-hand rule. Here, R_{Max} is the maximum deformation length of the droplet and θ is the auxiliary variable associated with the representation of droplet surface using a cylindrical system. Further, $h(x)$ is the radius of the cross-section at the position x as shown in figure 1(*a*), which is a single-variable function of x that satisfies $h'(0) = 0,\ \ h(\pm R_{Max}) = 0$, and $|h'(\pm R_{Max})| = \infty$. Hereafter, regarding the terms 'axisymmetric' or 'axisymmetrical' in this article, the axis of axial symmetry represents the longitudinal axis of the 2-lobed ('dumbbell-like' shaped) droplets, not

the axis of rotational angular velocity $\boldsymbol{\omega}$. In other words, the axisymmetrical axis is the x-axis in figure 1(a), not the z-axis.

In the rotational frame fixed to the rotating droplet, the Navier–Stokes (NS) equation can be written as

$$\frac{\mathrm{D}\boldsymbol{u}}{\mathrm{D}t} = \frac{1}{\rho}\nabla \cdot \tilde{\boldsymbol{\sigma}} - \boldsymbol{\omega} \times (\boldsymbol{\omega} \times \boldsymbol{r}) - 2\boldsymbol{\omega} \times \boldsymbol{u} - \left(\frac{\mathrm{D}\boldsymbol{\omega}}{\mathrm{D}t}\right) \times \boldsymbol{r}, \tag{2.2}$$

where $\mathrm{D}/\mathrm{D}t$ and $\tilde{\boldsymbol{\sigma}}$ denote the material derivative and stress tensor, respectively. In the NS equation above, the body forces except for the centrifugal force, Euler force and Coriolis force, such as gravity, are neglected. As the droplet consists of an incompressible fluid, the density and volume of the droplet are conserved during its deformation. In order to obtain the stress-balance equation in the direction of $\boldsymbol{e}_x$, i.e. the longitudinal direction of the droplet, we calculate the volume integration of the NS equation over the right half of the droplet ($0 \leqslant x \leqslant R_{Max},\ 0 \leqslant r \leqslant h(x),\ 0 \leqslant \theta \leqslant 2\pi$), where $\boldsymbol{\omega} = (0, 0, \omega)^{\mathrm{T}}$ and $\boldsymbol{r} = (x, r\cos\theta, r\sin\theta)^{\mathrm{T}}$. Owing to the axial symmetry of the shape with respect to the x-axis and the assumption that the flow inside the droplet is axisymmetric, the integration of summation of the last two terms on the right-hand side of the NS equation within the cross-section of the droplet at the position x, $y^2 + z^2 \leqslant h(x)^2$, is along the y direction. Accordingly, the stress-balance equation of the 2-lobed droplet in the direction of $\boldsymbol{e}_x$ is obtained by calculating the volume integration of the terms of inertial force, internal force and centrifugal force in the NS equation within the right half of the droplet ($0 \leqslant x \leqslant R_{Max},\ 0 \leqslant r \leqslant h(x),\ 0 \leqslant \theta \leqslant 2\pi$). Using the generalised Stokes' theorem and the boundary condition, $\tilde{\sigma} \cdot \boldsymbol{n} = -\gamma\kappa\boldsymbol{n}$ on the surface, the stress-balance equation in the direction of $\boldsymbol{e}_x$ can be rewritten as

$$\begin{aligned}\rho \int_{V/2} \frac{\mathrm{D}^2}{\mathrm{D}t^2}\boldsymbol{r}\ r\,\mathrm{d}r\,\mathrm{d}\theta\,\mathrm{d}x\ =\ & \int_{C_0} \tilde{\boldsymbol{\sigma}} \cdot \boldsymbol{n}\,\mathrm{d}S - \gamma \int_{S_f} \boldsymbol{n}\kappa\,\mathrm{d}S + \rho \int_{C_0} \boldsymbol{n}\frac{1}{2}\omega^2(x^2 + y^2)\,\mathrm{d}S \\ & + \rho \int_{S_f} \boldsymbol{n}\frac{1}{2}\omega^2(x^2 + y^2)\,\mathrm{d}S,\end{aligned} \tag{2.3}$$

where C_0 is the central cross-section, S_f is the free surface of the right half of the droplet ($0 \leqslant x \leqslant R_{Max},\ 0 \leqslant \theta \leqslant 2\pi$), $\boldsymbol{n}$ is the outward unit normal vector to each integral region of surface integration, ρ and γ denote the density and coefficient of surface tension of the droplet, respectively, and κ is twice the mean curvature of the interface, which can be evaluated as $\kappa = 1/(h\ (1 + (\mathrm{d}h/\mathrm{d}x)^2)^{1/2}) - (\mathrm{d}^2h/\mathrm{d}x^2)/(1 + (\mathrm{d}h/\mathrm{d}x)^2)^{3/2}$. Supplemental explanations of the derivation of (2.3) are provided in appendix A. Although (2.3) is a vector equation, the y and z components of each integral over S_f in (2.3) become 0 owing to the axial symmetry of the shape with respect to the x-axis. The y and z components of each integral over C_0 in (2.3) are also 0 because $\boldsymbol{n}$ is equal to $-\boldsymbol{e}_x$ on C_0. By substituting the stress tensor in the cylindrical coordinate (Landau & Lifshits 1959) and following Eggers & Dupont (1994) and Eggers & Fontelos (2005), the integral of $\tilde{\boldsymbol{\sigma}} \cdot \boldsymbol{n}$ over C_0 can be evaluated by assuming that the internal flow is axisymmetric. The integrals over S_f can be calculated using $\boldsymbol{n} = (-\mathrm{d}h/\mathrm{d}x, \cos\theta, \sin\theta)^{\mathrm{T}}/(1 + (\mathrm{d}h/\mathrm{d}x)^2)^{1/2}$ and $\mathrm{d}S = h\sqrt{1 + (\mathrm{d}h/\mathrm{d}x)^2}\,\mathrm{d}\theta\,\mathrm{d}x$ over the free surface. Using these, each term of (2.3) is explicitly calculated and the stress-balance equation in the direction of $\boldsymbol{e}_x$, i.e. the longitudinal direction of the 2-lobed droplet in rotation, can be shown to be

$$\frac{\mathrm{d}^2}{\mathrm{d}t^2}\left(\frac{1}{2}mX_G\right) = \frac{1}{2}mX_G\omega^2 + \pi\left[\gamma\left(H_{mid}^2 \cdot \kappa|_{H_{mid}} - 2H_{mid}\right) + 6\eta H_{mid}\frac{\mathrm{d}H_{mid}}{\mathrm{d}t}\right], \tag{2.4}$$

where η is the coefficient of viscosity, m is the total mass of the droplet, H_{mid} is the radius of the central cross-section and X_G denotes the distance between the central cross-section and the centre of gravity of each lobe, which can be evaluated as $mX_G/2 = \int_0^{R_{Max}} \rho\pi x h(x)^2 \,\mathrm{d}x$.

Furthermore, by calculating the volume integration of the torque generated by the Coriolis and Euler forces of the NS equation around the z axis, the conservation of angular momentum is expressed as

$$I_{zz}\frac{\mathrm{d}\omega}{\mathrm{d}t} + \omega\frac{\mathrm{d}I_{zz}}{\mathrm{d}t} = \Delta L(t) \simeq 0, \tag{2.5}$$

where I_{zz} is the moment of inertia of the right half of the droplet around the z-axis, which is evaluated as $I_{zz} = \int_{V/2} \rho(x^2 + y^2)\,\mathrm{d}x\,\mathrm{d}y\,\mathrm{d}z = \int_0^{R_{Max}} \int_0^{2\pi} \int_0^{h(x)} \rho(x^2 + r^2\cos^2\theta) r\,\mathrm{d}r\,\mathrm{d}\theta\,\mathrm{d}x$. By calculating this integration with respect to r and θ, I_{zz} is written such that $I_{zz} = \int_0^{R_{Max}} \rho\pi(x^2 h(x)^2 + h(x)^4/4)\,\mathrm{d}x$. $\Delta L(t)$ represents a slight increase in the angular momentum that corresponds to a small perturbation applied to the system, and $\Delta L(t) = 0$ almost every time.

Following Brown & Scriven (1980), we non-dimensionalise the angular velocity ω, time t, the distance between the central cross-section and an arbitrary cross-section x, the maximum deformation length R_{Max}, and the radius of the central cross-section H_{mid} using the reference constants ω_0 and R_0 such that

$$\omega = \omega_*\omega_0, \quad t = t_*/\omega_0, \quad x = R_0 x_*, \quad R_{Max} = R_{Max*}R_0, \quad \text{and} \quad H_{mid} = H_{mid*}R_0, \tag{2.6a–e}$$

where R_0 is the radius of a spherical drop of the same volume and ω_0 is the smallest eigenfrequency of the spherical harmonic oscillation of the drop, which is defined as $\sqrt{8\gamma/(\rho R_0^3)}$ (Rayleigh 1879; Landau & Lifshits 1959). Hereafter, the symbols with an asterisk $*$ denote the non-dimensionalised variables. As the differential operators $\mathrm{d}/\mathrm{d}t$ and $\mathrm{d}/\mathrm{d}x$ are rewritten as $\omega_0(\mathrm{d}/\mathrm{d}t_*)$ and $(1/R_0)(\mathrm{d}/\mathrm{d}x_*)$, respectively, the dimensionless forms of (2.4) and (2.5) can be obtained as follows:

$$\frac{\mathrm{d}^2}{\mathrm{d}t_*^2}x_{g*} = x_{g*}\omega_*^2 - H_{mid*} - H_{mid*}^2\left.\frac{\mathrm{d}^2 h_*(x_*)}{\mathrm{d}x_*^2}\right|_{x_*=0} + \frac{6\eta R_0\omega_0}{\gamma}H_{mid*}\frac{\mathrm{d}H_{mid*}}{\mathrm{d}t_*} \tag{2.7}$$

and

$$I_{zz*}\frac{\mathrm{d}\omega_*}{\mathrm{d}t_*} + \omega_*\frac{\mathrm{d}I_{zz*}}{\mathrm{d}t_*} = 0, \tag{2.8}$$

where $x_{g*} = 8\int_0^{R_{Max*}} x_* h_*(x_*)^2\,\mathrm{d}x_*$.

As (2.7)–(2.8) include terms calculated using the entire shape of the droplet, the entire shape of the droplet should be explicitly determined throughout the entire process of deformation. In this paper, we determine the cross-sectional radius of the droplet $h_*(x_*)$ as a mathematical function, i.e. the Cassinian oval curve, by focusing on the similarity of the shapes. A Cassinian oval is a quartic plane curve defined as

$$(Ax_*^2 + z_*^2)^2 - (Au_*^2 - v_*^2)(Ax_*^2 - z_*^2) - Au_*^2 v_*^2 = 0 \ \ (Au_* > v_* > 0). \tag{2.9}$$

The shape of the curve, up to mathematical similarity, depends on two dimensionless parameters: $k = u_*/v_*$ and A. When $k \geqslant 1$, the curve is a single connected loop. It is convex for $1 \leqslant k \leqslant \sqrt{3/A}$ and 2-lobed for $k > \sqrt{3/A}$ (Basset 1901), as described in figure 1(*b*) (refer to appendix B for details). The limiting case of $k \to \infty$ of (2.9)

is an ∞-like shaped curve that has a singular point at the origin and the curve approaches $z_* = \pm\sqrt{A}x_*$ at the origin (the red curve in figure 1*b*). In other words, when k approaches ∞ and the neck region of the Cassinian droplet pinches off, the vicinity of the midpoint of the Cassinian droplet is approximated by cones with the apex angle $\phi = 2\arctan(\sqrt{A})$, i.e. A is a parameter expressing the degree of sharpness of the neck region at the moment the neck region of the Cassinian droplet pinches off. We infer that $A < 1 = (\arctan 45^\circ)^2$ by observing the shape of actual 2-lobed droplets at the moment the droplet breaks up (figure 10*h* of Wang *et al.* (1994) and figure 7*G* of Rhim *et al.* (1990)); however, we need not to limit the range of the value of A here. The value of the parameter A is fixed within the process of deformation and breakup of the Cassinian droplet, and the value is determined in § 3.

As the Cassinian oval curve expressed by (2.9) intersects the x_*-axis and z_*-axis at $(\pm u_*, 0)$ and $(0, \pm v_*)$, respectively, the parameters u_* and v_* correspond to R_{Max*} and H_{mid*}, respectively. In the present study, the shape of the interface of a 2-lobed droplet is determined as a solid of revolution generated by a Cassinian oval curve in order to have axial symmetry with respect to the x_*-axis such that $(Ax_*^2 + y_*^2 + z_*^2)^2 - (Au_*^2 - v_*^2)(Ax_*^2 - y_*^2 - z_*^2) - Au_*^2v_*^2 = 0$. By substituting $\sqrt{y_*^2 + z_*^2} = h_*(x_*)$ into this equation and solving for $h_*(x_*)$, we obtained the dimensionless radius profile of the Cassinian droplet such that

$$h_*(x_*) = \sqrt{\tfrac{1}{2}(-Au_*^2 + v_*^2 - 2Ax_*^2 + \sqrt{(Au_*^2 + v_*^2)^2 + 8A(Au_*^2 - v_*^2)x_*^2})}. \tag{2.10}$$

Subsequently, x_{g*} is calculated as

$$x_{g*} = 8\int_0^{u_*} x_* \cdot h_*(x_*)^2 \,\mathrm{d}x_* = \frac{1}{3A}(A^2u_*^4 + 4Au_*^2v_*^2 + v_*^4), \tag{2.11}$$

and the dimensionless moment of inertia I_{zz*} can be expressed as a function of u_* and v_* (refer to appendix C). Substituting the formulas (2.10) and (2.11) into (2.7), the dimensionless form of the stress-balance equation of a Cassinian drop is derived as

$$\begin{aligned}\frac{\mathrm{d}^2}{\mathrm{d}t_*^2}\left(\frac{1}{3A}(A^2u_*^4 + 4Au_*^2v_*^2 + v_*^4)\right) = {} & \omega_*^2\,\frac{1}{3A}(A^2u_*^4 + 4Au_*^2v_*^2 + v_*^4) \\ & - \frac{v_*(A(1+A)u_*^2 - (3A-1)v_*^2)}{Au_*^2 + v_*^2} \\ & + \frac{6\eta R_0\omega_0}{\gamma}\cdot v_*\frac{\mathrm{d}v_*}{\mathrm{d}t_*}.\end{aligned} \tag{2.12}$$

As there are three dependent variables, u_*, v_*, and ω_*, in the system, the deformation of a 2-lobed droplet can be quantitatively evaluated using (2.12), the conservation of angular momentum, and the volume conservation equation.

As expressed in (2.1), the droplet is determined as a solid of revolution generated by a Cassinian oval curve, and the shape of an arbitrary cross-section of the droplet is a circle. Therefore, the 2-lobed shape of the elliptical cross-section observed immediately after the transition point from the equilibrium shape that is axisymmetric with respect to the axis of rotation (e.g. figure 10 in Wang *et al.* (1994) and figure 7 in Rhim *et al.* (1990)) is not expressed by the proposed model.

3. The stationary solution and its linear stability

In this section, we demonstrate the existence of stationary solutions of (2.8) (2.12) and perform a linear stability analysis of the solutions. Henceforth, $k = u_*/v_*$, which was introduced in the previous section and represents the ratio of the maximum deformation length to the radius of the central cross-section of a Cassinian droplet, is treated as one of the dependent variables of the governing equations. Substituting u_*/k for v_* into the integral $\int_0^{u_*} h_*(x_*)^2\,\mathrm{d}x_*$, we obtain the equation of dimensionless volume conservation:

$$\begin{aligned}\frac{2}{3} &= \int_0^{u_*} h_*(x_*)^2\,\mathrm{d}x_* = \frac{1}{12}u_*(-Au_*^2+3v_*^2)\\ &\quad+\frac{(Au_*^2+v_*^2)^2}{8\sqrt{2A(Au_*^2-v_*^2)}}\log_e\left(\frac{3Au_*^2-v_*^2+2u_*\sqrt{2A(Au_*^2-v_*^2)}}{Au_*^2+v_*^2}\right)\\ &= u_*^3\left[\frac{1}{12}\left(-A+\frac{3}{k^2}\right)+\frac{1}{8\sqrt{2}}\frac{(Ak^2+1)^2}{k^3\sqrt{A(Ak^2-1)}}\right.\\ &\quad\left.\times\log_e\left(\frac{3Ak^2-1+2\sqrt{2}k\sqrt{A(Ak^2-1)}}{Ak^2+1}\right)\right].\end{aligned}\tag{3.1}$$

Solving (3.1) for u_*, each variable, $u_* = R_{Max}/R_0$ and $v_* = H_{mid}/R_0 = u_*/k$, can be expressed as a single-variable function of k with the parameter A.

When $u_*(k;A)$ and $v_*(k;A)$ are substituted into (2.8) and (2.12), each component is also expressed as a single-variable function of k. Hereafter, the symbols with $(k;A)$ denote variables in which $u_*(k;A)$ and $v_*(k;A)$ have been substituted. Subsequently, the first-order coupled differential equations of k, ω_*, and ℓ $(=\mathrm{d}k/\mathrm{d}t_*)$ can be obtained as follows:

$$\frac{\mathrm{d}k}{\mathrm{d}t_*} = \ell,\tag{3.2}$$

$$\frac{\mathrm{d}\omega_*}{\mathrm{d}t_*} = -\omega_*\frac{I'_{zz*}(k;A)}{I_{zz*}(k;A)}\ell,\tag{3.3}$$

$$\frac{\mathrm{d}\ell}{\mathrm{d}t_*} = -\frac{x''_{g*}(k;A)}{x'_{g*}(k;A)}\ell^2+\frac{x_{g*}(k;A)}{x'_{g*}(k;A)}\omega_*^2-\frac{K(k;A)}{x'_{g*}(k;A)}+N\cdot\frac{v_*(k;A)v'_*(k;A)}{x'_{g*}(k;A)}\ell,\tag{3.4}$$

where $K(k;A)$ denotes the second term of the right-hand side of (2.12) and the prime symbols $'$ and $''$ are the first and second derivatives with respect to k, respectively. N is a dimensionless constant expressed as

$$N = \frac{6\eta R_0\omega_0}{\gamma} = 12\sqrt{2}\frac{\eta}{\sqrt{\rho\gamma R_0}} = 12\sqrt{2}Oh,\tag{3.5}$$

where Oh is the Ohnesorge number calculated using R_0, which is the radius of a spherical drop of the same volume.

Solving (3.2)–(3.4) with the left-hand side of each equation set to 0, the set of stationary solutions can be obtained as

$$\forall k\in[\sqrt{3/A},\infty),\quad \omega_* = \omega_{*,s}(k;A),\quad \ell = 0,\tag{3.6a–c}$$

where $\omega_{*,s}(k;\,A)$ is the positive solution of $x_{g*}(k;\,A)\cdot\omega_*^2 - K(k;\,A) = 0$, which is expressed as

$$\omega_{*,s}(k;\,A) = \sqrt{\frac{3Av_*(A(1+A)u_*^2 - (3A-1)v_*^2)}{(Au_*^2+v_*^2)(A^2u_*^4+4Au_*^2v_*^2+v_*^4)}}\,\Bigg|_{\substack{u_*=u_*(k;A)\\ v_*=v_*(k;A)}}. \tag{3.7}$$

$\omega_{*,s}(k;\,A)$ and $u_*(k;\,A)$ are functions of k with the parameter A, and full forms are expressed in appendix C. When the value of parameter A is determined, we can calculate one corresponding value of k for a given value of $u_*(k;\,A)$, and corresponding value of $\omega_{*,s}(k;\,A)$ is calculated. In other words, using (3.7) we can draw a plot of parametric equations $(\omega_{*,s}(k;\,A),\,u_*(k;\,A))$ by changing the values of k within the range of $k > \sqrt{3/A}$, the range of k within which a Cassinian droplet has a 2-lobed shape. The graphs are described in figure 2.

In order to investigate the stability of the stationary solution against a small perturbation, we now perform a linear stability analysis. An example of a perturbation is a slight increase in the angular momentum, i.e. $\Delta L(t)$ in (2.5). Linearising (3.2)–(3.4) at $(k,\,\omega_*,\,\ell) = (k,\,\omega_{*,s}(k;\,A),\,0)$, we obtain the Jacobian matrix $\boldsymbol{J}$ such that

$$\begin{aligned}\boldsymbol{J} &= \begin{pmatrix} 0 & 0 & 1 \\ -\omega_*\left(\dfrac{I'_{zz*}}{I_{zz*}}\right)'\ell & -\left(\dfrac{I'_{zz*}}{I_{zz*}}\right)\ell & -\left(\dfrac{I'_{zz*}}{I_{zz*}}\right)\omega_* \\ \dfrac{\partial}{\partial k}(\text{RHS of (3.4)}) & 2\omega_*\left(\dfrac{x_{g*}}{x'_{g*}}\right) & -2\ell\left(\dfrac{x''_{g*}}{x'_{g*}}\right)+N\dfrac{v_*v'_*}{x'_{g*}} \end{pmatrix}\Bigg|_{\substack{\omega_*=\omega_{*,s}(k;A),\\ \ell=0}} \\ &= \begin{pmatrix} 0 & 0 & 1 \\ 0 & 0 & -\left(\dfrac{I'_{zz*}}{I_{zz*}}\right)\omega_{*,s} \\ \omega_{*,s}^2\left(\dfrac{x_{g*}}{x'_{g*}}\right)' - \left(\dfrac{K}{x'_{g*}}\right)' & 2\omega_{*,s}\left(\dfrac{x_{g*}}{x'_{g*}}\right) & N\dfrac{v_*v'_*}{x'_{g*}} \end{pmatrix}. \end{aligned} \tag{3.8}$$

The eigenvalues of $\boldsymbol{J}$ are expressed as

$$\lambda_0 = 0, \quad \lambda_\pm = \frac{J_{33} \pm \sqrt{J_{33}^2 + 4(J_{31}+J_{23}J_{32})}}{2}, \tag{3.9a,b}$$

where J_{ij} is the $(i,\,j)$ component of the matrix $\boldsymbol{J}$. If both $\mathrm{Re}[\lambda_+]$ and $\mathrm{Re}[\lambda_-]$ are negative, the stationary solution is stable. As $x_{g*}(k;\,A)$ increases and $v_*(k;\,A)$ decreases with an increase in k, $J_{33} < 0$ for an arbitrary value of k. Therefore, the condition of linear stability is equivalent to

$$D(k;\,A) := J_{31} + J_{23}J_{32} < 0, \tag{3.10}$$

regardless of the value of N. As $D(k;\,A)$ is a monotonically increasing function of k (refer to the latter part of appendix C), there exists a critical value $k_{crit,A}$ that satisfies $D(k_{crit,A};\,A) = 0$ for each value of the parameter A. Subsequently, according to the proposed model, if and only if $k > k_{crit,A}$, the stationary solution is unstable for the corresponding A. In other words, the condition of linear stability only depends on the

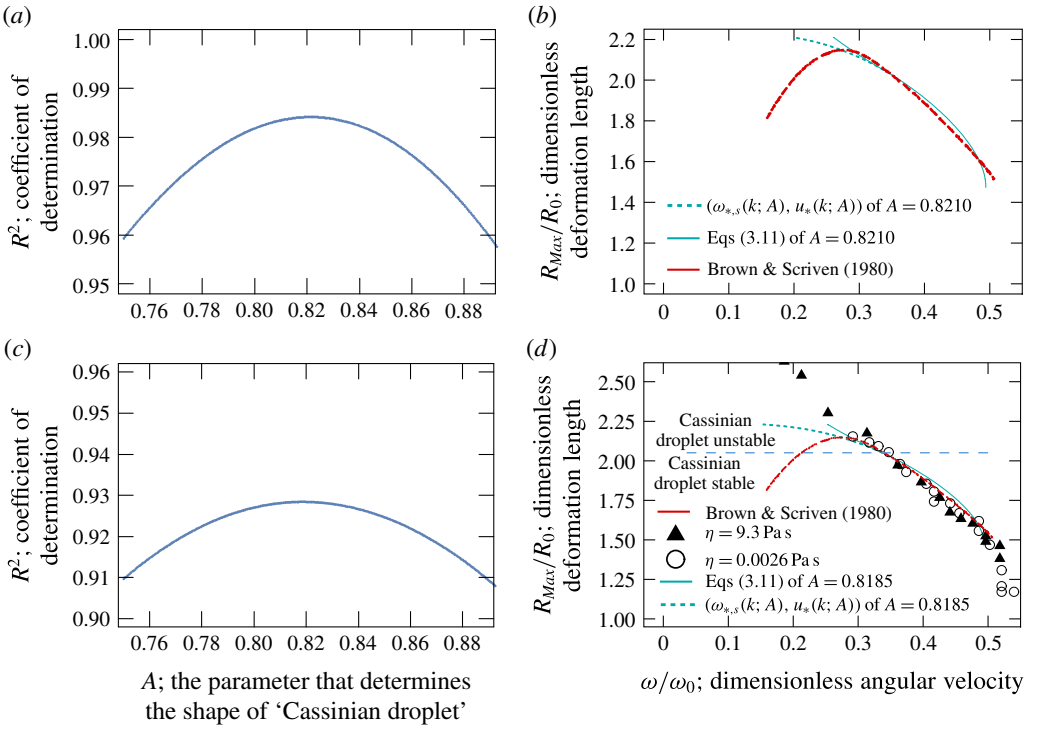

FIGURE 2. (Colour online) Results of least squares fittings using the ascending part of the 2-lobed branch of Brown and Scriven's numerical calculation (figure 6 of Brown & Scriven (1980), red lines shown in panels (*b*) and (*d*)) and the experimentally obtained scatter plot (figure 4 of Tanaka *et al.* 2013). (*a*,*b*) Least squares regression between (3.11) and Brown and Scriven's numerical solution. The plot of Brown and Scriven's solution is fitted best when $A = 0.821$. The coefficient of determination, R^2, is approximately 0.984. (*c*,*d*) Result of the least squares fitting using the experimentally obtained scatter plot as the dataset. The experimental result is very well approximated by (3.11) when $A = 0.8185$. The coefficient of determination is approximately 0.928. Panel (*d*) is created by using the data provided by authors of Tanaka *et al.* (2013). The entire data are shown in figure 4 of Tanaka *et al.* (2013).

ratio of the maximum deformation length to the radius of the central cross-section of the droplet, regardless of its physical properties, i.e. η, γ, ρ and R_0. By numerically solving the inequality (3.10), $k_{crit,A}$ is calculated for each value of A. We discuss the rate of growing of a minute shift of (ω_*, u_*) from an equilibrium point under the condition that the stationary solution (3.6) is unstable. The Taylor expansion of $\lambda_+ = (J_{33} + \sqrt{J_{33}^2 + 4D(k;A)})/2$ at $k = k_{crit,A}$ that satisfies $D(k_{crit,A}; A) = 0$ is calculated as $\lambda_+ = -D/J_{33} + (1/J_{33})(D/J_{33})^2 - (2/J_{33}^2)(D/J_{33})^3 + O((D/J_{33})^4)$. As J_{33} is negative and proportional to N, $\mathrm{Re}[\lambda_+]$ becomes larger as $N = 12\sqrt{2}\eta/\sqrt{\rho\gamma R_0} = 12\sqrt{2}Oh$ becomes smaller under the condition that the stationary solution (3.6) is unstable. Therefore, a minute shift of (ω_*, u_*) begins to grow at a rate inversely proportional to the Ohnesorge number.

In order to determine the optimal value of the parameter A, we perform a least square regression with two preceding studies: Brown and Scriven's numerical calculation and an experimental study (Tanaka *et al.* 2013). The dataset used for

regression with (Brown & Scriven 1980) is a part of Brown and Scriven's solution of 2-lobed equilibrium shapes satisfying $0.305 \leqslant \omega/\omega_0 < 0.506$, which belongs to the region where the angular momentum does not decrease as the angular velocity of rotation decreases (the graph displayed in figure 6 of Brown & Scriven (1980)). The dataset used for the regression with the experimental study is a part of the experimental data presented in figure 4 of Tanaka *et al.* (2013), an experimental study on measuring viscosity by using the breakup behaviour of a levitated droplet, and is provided by the authors of the paper. The dataset used for the regression with the experimental study consists of points on the 2-lobed branch of experimentally obtained scatter plot of R_{Max}/R_0 versus ω/ω_0 of $\eta = 0.0026$ Pa s satisfying $\omega/\omega_0 < 0.525$ and these of R_{Max}/R_0 versus ω/ω_0 of $\eta = 9.3$ Pa s satisfying $0.35 < \omega/\omega_0 < 0.525$ that belongs to the stable region in the proposed model for all the values of A tested. Here, in this study, the 2-lobed branch of the experimentally obtained scatter plot is a set of points that are located close to the ascending part of the 2-lobed brunch of Brown and Scriven's solution and that are not close to the transition point to the 2-lobed shape out of the points on experimentally obtained scatter plot (shown in figure 4 of Tanaka *et al.* (2013)). According to the above definition, the dataset used for the regression with the experimental study is obtained by removing the four circles that are located in the bottom right and the triangles that are located in the range of $\omega/\omega_0 < 0.35$ from the scatter plot shown in 2(*d*). The regression function is defined as

$$\left.\begin{array}{ll} \omega_* = \begin{cases} \omega_{*,s}(k; A) & (k \leqslant k_{crit,A}), \\ \omega_{*,s}(k_{crit,A}; A) I_{zz*}(k_{crit,A}; A)/I_{zz*}(k; A) & (k > k_{crit,A}), \end{cases} \\ R_{Max*} = u_*(k; A). \end{array}\right\} \tag{3.11}$$

Here, $\omega_{*,s}(k; A)$ is the stationary solution of the rotation rate that is expressed in (3.7). This regression function corresponds to the situation where the maximum deformation length of the droplet increases while following the locus of a linearly stable stationary solution by quasi-statically adding the angular momentum, and the angular momentum is conserved when $R_{Max*} = u_* > u_{*crit,A}$.

We show the results of the least squares regression in figure 2. As shown in figure 2(*a*,*b*), Brown and Scriven's solution of 2-lobed equilibrium shapes satisfying $0.305 \leqslant \omega/\omega_0 < 0.506$ is fitted best by (3.11) when $A = 0.8210$. On the other hand, the experimentally obtained scatter plot (figure 4 of Tanaka *et al.* (2013)) is fitted best by (3.11) when $A = 0.8185$ (figure 2*c*,*d*). For each least squares regression, the coefficient of determination, which is defined as $R^2 = 1 - \sum_{data}(\omega_*(k; A) - \omega_{data})^2 / \sum_{data}(\overline{\omega}_{data} - \omega_{data})^2$, is maximised at the value of A shown above. Here, $\omega_*(k; A)$ is the angular velocity expressed in (3.11). ω_{data} is the ω-component of each element of the dataset for regression and $\overline{\omega}_{data}$ is the mean of ω_{data}. The set of ω_{data} is defined for each regression dataset. The ascending region of the 2-lobed brunch of Brown and Scriven's solution is fitted best by (3.11) and takes a maximum value of 0.984 when $A = 0.8210$, and experimental data used for regression provided by Tanaka *et al.* (2013) are fitted best by (3.11) with a maximum value of 0.928 when $A = 0.8185$. As the coefficient of determination defined in the present study becomes larger, a better fit between the data and the result obtained from the Cassinian droplet model is provided. As mentioned above, the maximum value of R^2 obtained from the regression with Brown and Scriven's solution ($R^2 \simeq 0.984$) is larger than the maximum value of R^2 obtained from the regression with

experiment (Tanaka *et al.* 2013) ($R^2 \simeq 0.928$). Besides, as shown in figure 2(*d*) and mentioned in the original paper (Tanaka *et al.* 2013), the experimentally obtained dataset used for the regression is very consistent with Brown and Scriven's solution. In other words, most of points of the experimental dataset lie very close to the ascending part of the 2-lobed brunch of Brown and Scriven's solution (figure 2*d*). From above two reasons, we adopt the value of A that is determined form Brown and Scriven's solution as the optimal value of A, A_{opt}. Therefore, in this study, the optimal value of the parameter A is determined as

$$A_{opt} = 0.8210. \tag{3.12}$$

In terms of A_{opt}, the boundary of the linear stability of the stationary solutions is derived as

$$\left.\begin{gathered} k_{crit,A_{opt}} \simeq 5.379, \quad \omega_{*,crit,A_{opt}} \simeq 0.337, \quad u_{*,crit,A_{opt}} \simeq 2.050, \quad v_{*,crit,A_{opt}} \simeq 0.381, \\ 2\pi I_{zz*}(k_{crit,A_{opt}}; A_{opt}) \cdot \omega_{*,crit,A_{opt}} \simeq 2.046, \end{gathered}\right\} \tag{3.13}$$

by solving the inequality (3.10).

The horizontal broken line drawn in figure 2(*d*) is the boundary of the linear stability of the stationary solution obtained in the present study, and the angular momentum of the Cassinian droplet rotating at the rate corresponding to the stationary solution becomes maximum at $k_{crit,A_{opt}}$ (refer to appendix C), and the dimensionless critical values of the rotation rate and deformation length are displayed above. In the graph obtained in Brown & Scriven (1980), the dimensionless angular momentum is maximised at $(\omega_*, R_{Max*}) \approx (0.31, 2.10)$. The maximum value is approximately equal to 2.02 (Brown & Scriven 1980), which is close to the value shown in (3.13). In actual situations, as shown in figure 2(*d*), the scatter plots of R_{Max}/R_0 versus ω/ω_0 appear to protrude slightly from Brown and Scriven's solution around the point $(\omega_*, R_{Max*}) = (0.332, 2.091)$. A similar deforming behaviour is shown more clearly in figure 7 of Wang *et al.* (1994), which describes the deformation and breakup of a droplet consisting of low-viscosity silicone oil owing to rotation, and the critical point is $(\omega_*, R_{Max*}) \approx (0.33, 2.07)$. Moreover, as mentioned in Baldwin *et al.* (2015) and Butler *et al.* (2011), artificial tektites are obtained numerically or experimentally by solidifying steadily rotating deformed drops, and if an artificial tektite belongs to the 2-lobed family, the value of H_{mid}/R_{Max} of each tektite, which is the same as $1/k$, is in the range of 0.2 or more. In the present study, the stability limit of H_{mid}/R_{Max} is $1/k_{crit,A_{opt}} = 1/5.379 \simeq 0.186$. Hence, the result of stability analysis of the present study is consistent with those of the aforementioned theoretical and experimental studies. Thus, it can be concluded that, even when the deformation length increases quasi-statically via the addition of angular momentum to the droplet, if it becomes slightly larger than $R_0 \cdot u_{*,crit,A_{opt}}$, the deformation length of the Cassinian droplet increases unsteadily and breakup occurs. By utilising the Cassinian droplet model, if the angular momentum $I_{zz*} \cdot \omega_*$ is conserved when the dimensionless deformation length $u_* = R_{Max*} > 2.05$, the breakup limit of $R_{Max*} = u_*$ and ω_* are calculated. When k approaches infinity under the above assumption, $\omega_*(k; A_{opt})$, $u_*(k; A_{opt})$, and $v_*(k; A_{opt})$ approach the breakup limit:

$$\omega_{*,break,A_{opt}} \simeq 0.249, \quad u_{*,break,A_{opt}} \simeq 2.24, \quad v_{*,break,A_{opt}} = 0. \tag{3.14a–c}$$

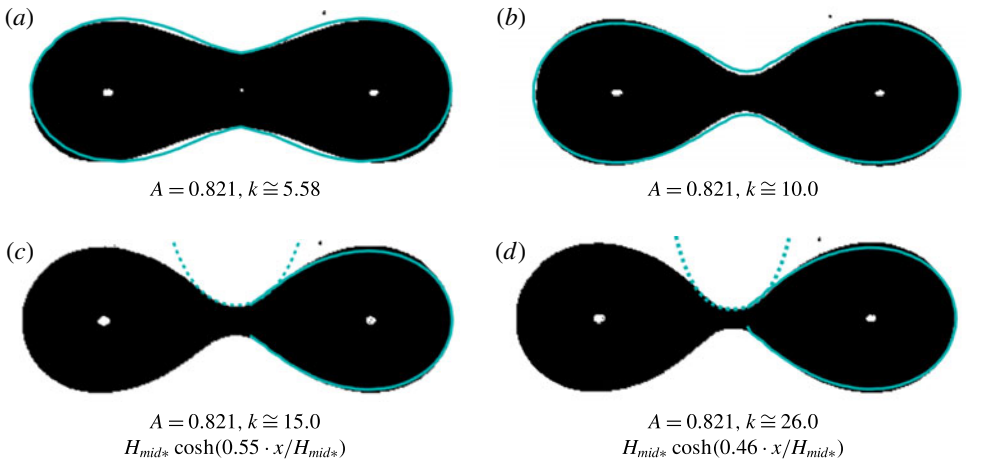

FIGURE 3. (Colour online) The outline shape of an experimentally stretched low-viscosity 2-lobed droplet ($\eta = 0.0026$ Pa s) is compared with a corresponding Cassinian oval curve $z_* = h_*(x_*;\ k,\ A_{opt})$. (*a*) The Cassinian oval curve of $A_{opt} = 0.821$ (solid lines) fits the outline shape of the experimentally stretched 2-lobed droplet very well. The rotation rate and deformation length of the Cassinian droplet are calculated as $(\omega_*,\ R_{Max*}) \simeq (0.331, 2.06)$ using (3.11), and this calculated result closely approximates the deformation state $(\omega_*, R_{Max*}) = (0.332, 2.091)$ in the experiment. (*b*)–(*d*) Three snapshots capturing the low-viscosity droplet immediately before its neck region pinches off. Although the outline shape of the low-viscosity droplet is not fitted well by the Cassinian oval curve itself for snapshots (*c*,*d*), the outline shape of the droplet is expressed by the combination of the breakup limit of the Cassinian oval curve and the interpolating hyperbolic cosine function (the broken line) smoothly connected with the Cassinian oval. Each snapshot is provided by the authors of Tanaka *et al.* (2013), and each snapshot is binarised by authors of this paper in order to clarify the outline shape of the droplet.

We compared the Cassinian oval curve of A_{opt} and the outline shape of an experimentally stretched low-viscosity droplet ($\eta = 0.0026$ Pa s, which is provided by the authors of Tanaka *et al.* (2013)). As shown in figure 3(*a*), the Cassinian oval curve of A_{opt} fits the outline shape of the actual low-viscosity droplet very well. At the moment the snapshot (*a*) is captured, the values of the dimensionless rotation rate and dimensionless deformation length of the Cassinian droplet are $(\omega_*,\ R_{Max*}) = (0.331,\ 2.06)$, and the closest point in the experimental scatter plot of $\eta = 0.0026$ Pa s is $(\omega_*,\ R_{Max*}) = (0.332,\ 2.091)$. Slightly before the low-viscosity droplet breaks up (figure 3*b*), the Cassinian oval curve and the outline shape of the actual droplet also overlap well, although there is a slight misalignment at the vicinity of the central cross-section. For snapshot (*b*), $(\omega_*,\ R_{Max*})$ of the corresponding Cassinian droplet of A_{opt} is (0.275, 2.177), and the closest point in the experimental scatter plot of $\eta = 0.0026$ Pa s (displayed in figure 2*d*) is $(\omega_*, R_{Max*}) = (0.292, 2.153)$ and the closest point in the plot of Brown and Scriven's solution is $(\omega_*, R_{Max*}) \approx (0.28, 2.15)$, which is located close to the summit of Brown and Scriven's solution. Thus, we have demonstrated that the process of deformation of the Cassinian droplet is consistent with both the experimental observations and Brown and Scriven's numerical calculation.

Furthermore, the relationship between angular momentum and rotation rate of rotating Cassinian droplet, i.e. the parametric plot of $2\pi I_{zz*}(k;\ A_{opt}) \cdot \omega_{*,s}(k;\ A_{opt})$

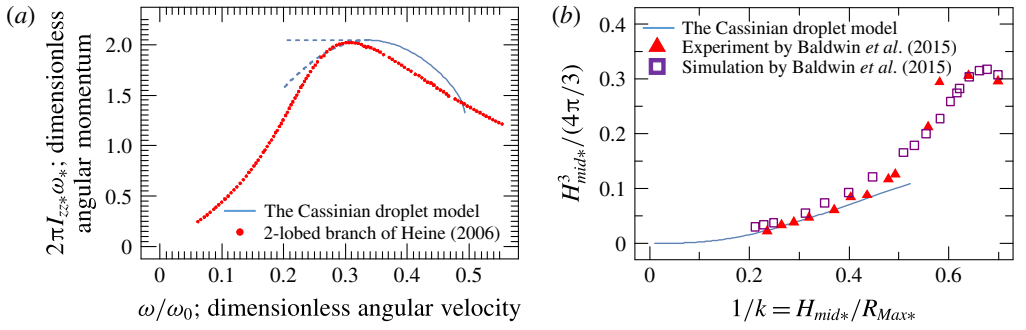

FIGURE 4. (Colour online) (*a*) Relationship between angular momentum and rotation rate of the droplet that has the equilibrium shape belonging to the 2-lobed branch computed in Heine (2006) and that of the proposed 'Cassinian droplet' of $A_{opt} = 0.821$ are compared. The scatter plot shown in panel (*a*) is created by reading off values from the 2-lobed branch of the computational result that is presented in figure 12 of Heine (2006). (*b*) The deformation of the Cassinian droplet is compared with the deformation of the actual droplet in rotation presented in Baldwin *et al.* (2015). The solid line shows $v_*^3/(4\pi/3)$ of the Cassinian droplet of $A_{opt} = 0.821$, which models 2-lobed droplets of circular cross-section, and is consistent with the deforming behaviour of the 2-lobed droplet obtained from Baldwin *et al.* (2015). The scatter plot shown in panel (*b*) is created by reading off values from figure 4 of Baldwin *et al.* (2015).

versus $\omega_{*,s}(k;\, A_{opt})$, is compared with the numerical calculation presented in Heine (2006), which reproduced the relationship between the angular momentum and rotation rate of the droplet that has the equilibrium shape presented in figure 4 of Brown & Scriven (1980). As shown in figure 4(*a*), the parametric plot of $(\omega_{*,s}(k;\, A_{opt}),\ 2\pi I_{zz*}(k;\, A_{opt})\omega_{*,s}(k;\, A_{opt}))$ obtained by the Cassinian droplet model well reproduces the qualitative tendency of the diagram: $2\pi I_{zz*}(k;\, A_{opt})\omega_{*,s}(k;\, A_{opt})$ also change increase to decrease as $\omega_{*,s}(k;\, A_{opt})$ decreases, and the maximum value of $2\pi I_{zz*}(k;\, A_{opt}) \cdot \omega_{*,s}(k;\, A_{opt})$ is almost equal to the maximum value of the angular momentum calculated in Heine (2006). Although the plot of $2\pi I_{zz*}(k; A_{opt}) \cdot \omega_{*,s}(k; A_{opt})$ as a function of $\omega_{*,s}(k; A_{opt})$ does not overlap quantitatively and precisely with the corresponding results presented in the previous studies, the relationship between the characteristic quantities of 2-lobed 'dumbbell-like' droplets calculated in this study are consistent with the result of the experimental study (Baldwin *et al.* 2015) (figure 4*b*). According to these observations and the really good approximate consistency observed between the result of the present study and results of the previous studies as expressed in figure 2 and figure 3, we conclude that the Cassinian oval curve is an appropriate approximate solution of the entire shape of the interface of rotating 2-lobed droplets.

Particularly in the case of low-viscosity droplets, the entire process of deformation of 2-lobed droplets including immediately before breakup is very well reproduced by the proposed model. If $N = (6\eta R_0\omega_0)/\gamma \to 0$, and if the angular momentum $L_* = I_{zz*}\omega_*$ is conserved under the condition $u_* > u_{crit*}$, the exact solutions of (3.2)–(3.4) can be derived. As the ratio k $(= R_{Max}/H_{mid})$ is a monotonically increasing function of t_*, the inverse function $t_*(k)$ exists and (3.2)–(3.4) can be transformed into

$$-\frac{\mathrm{d}^2 t_*}{\mathrm{d}k^2} = -\frac{x''_{g*}}{x'_{g*}}\left(\frac{\mathrm{d}t_*}{\mathrm{d}k}\right) + \left(\frac{x_{g*}}{x'_{g*}}\left(\frac{L_{*crit}}{I_{zz*}}\right)^2 - \frac{K}{x'_{g*}}\right)\left(\frac{\mathrm{d}t_*}{\mathrm{d}k}\right)^3, \tag{3.15}$$

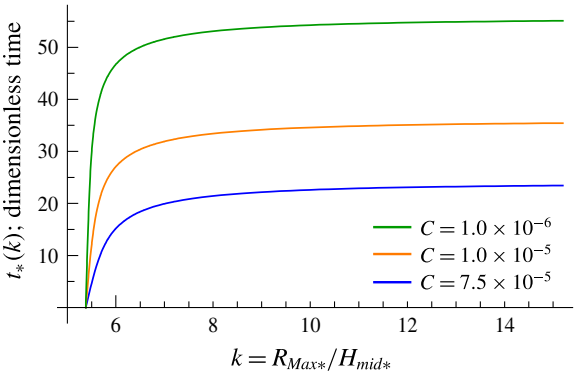

FIGURE 5. (Colour online) The solution of (3.16) is plotted for different values of the integral constant C in case of $A_{opt} = 0.821$. For each value of C, the limit $\lim_{k\to\infty} t_*(k)$, the time required for the extremely low-viscosity Cassinian droplet to reach breakup, is a finite value.

where $L_{*crit} := I_{zz*}(k_{crit,A}; A)\omega_{*,s}(k_{crit,A}; A)$ is the angular momentum of a stably rotating Cassinian drop whose dimensionless deformation length is $u_*(k_{crit,A}; A)$. The above equation is the Bernoulli differential equation, and therefore, its exact solution can be derived as

$$t_*(k) = \int_{k_0}^{k} \frac{x'_{g*}(\tilde{k}; A)}{\sqrt{\displaystyle\int_{k_0}^{\tilde{k}} \left[2x'_{g*}(\hat{k}; A)\left(x_{g*}(\hat{k}; A)(L^2_{*crit,A}/I^2_{zz*}(\hat{k}; A)) - K(\hat{k}; A)\right)\right] \mathrm{d}\hat{k} + C}}\, \mathrm{d}\tilde{k}. \tag{3.16}$$

From the above equation, the time required to achieve a certain value of k $(= R_{Max}/H_{mid})$ from the stability limit of the stationary solution can be evaluated. In figure 5, $t_*(k)$ is plotted for different values of C. C is a parameter related to the initial velocity of the centre of gravity of each lobe, and assumes a very small value in order to make $\mathrm{d}k/\mathrm{d}t_*$ close to 0 at $t_* = 0$. By using (3.16), it is possible to estimate the time required for the extremely low-viscosity droplet to reach breakup from the stability limit of the deformation length by evaluating $t_{*,break} = \lim_{k\to\infty} t_*(k)$. As an example, $t_{*,break} \approx 35.5$ in the case of $C = 1.0 \times 10^{-5}$. The reference constant of non-dimensionalisation is $\omega_0 \approx 533\ \mathrm{s}^{-1}$ if the physical properties of a low-viscosity droplet are $R_0 = 1.0$ mm, $\rho = 1210\ \mathrm{kg\ m}^{-3}$, $\gamma = 43\ \mathrm{mN\ m}^{-1}$, the time required for breakup is approximately equal to 0.066 s. It is demonstrated that the time during which the 2-lobed droplet of $\eta = 1.0$ Pa s deforms unstably until breakup occurs is less than 0.1 s in Tanaka *et al.* (2013). This fact is consistent with the calculation result presented here.

This breakup behaviour closely resembles the 'finite time singularity' in the jet breakup theory (e.g. Papageorgiou 1995); however, it appears that the breakup of rotating extremely low-viscosity droplets in finite time occurs via a different mechanism. Referring to the stress-balance equation ((2.4) or (2.7)), under the situation where extremely low-viscosity droplets in rotation deform unstably and significantly and break up, among the terms of inertia, centrifugal force and curvature of the droplet interface, the term of centrifugal force is relatively large, and the stress-balance equation is modified as (A function of k that takes a finite value) =

$(\eta/\sqrt{\gamma\rho R_0})H_{mid*}(\mathrm{d}H_{mid*}/\mathrm{d}t_*)$. Therefore, if $N = 12\sqrt{2}\eta/\sqrt{\gamma\rho R_0} \to 0$, $|\mathrm{d}H_{mid*}/\mathrm{d}t_*| \to \infty$ must occur. This mechanism, i.e. the balance of the centrifugal force and the term related to time derivative of the radius of the central cross-section, causes a sharp decrease in the central cross-section in the process by which an extremely low-viscosity droplet breaks up owing to rotation.

4. Summary and discussion

In this study, we proposed a simple model of rotating 2-lobed droplets by representing their outline shapes using the mathematical plane curves of Cassinian ovals (the Cassinian drop model). By continuously changing the values of their parameters, these curves can form various shapes from a peanut-like shape to an ∞-like shape, which are observed in the process of deformation of a 2-lobed droplet stretched in laboratories. We obtained the governing equation of deformation of a Cassinian drop and demonstrated that a stationary solution of the angular velocity exists for an arbitrary maximum deformation length. As a result of the linear stability analysis, it was demonstrated that the condition of linear stability depends only on the ratio of the maximum deformation length to the central cross-section of the Cassinian drop, regardless of the physical properties of the droplet, i.e. volume, density, coefficient of surface tension and viscosity. Furthermore, via comparisons with an experimental observation (Tanaka *et al.* 2013), it was observed that the set of linearly stable stationary solutions of A_{opt} was consistent with the behaviour of experimentally stretched 2-lobed droplets for a wide range of physical properties.

Further, we discuss the applicability of the Cassinian drop model to the breakup behaviour of 2-lobed droplets. In general, when a high-viscosity droplet breaks up, a liquid filament is formed around its midpoint as its deformation length rapidly increases. In case of low-viscosity droplets, a liquid filament is not formed, and the radius of the central cross-section decreases sharply. Conversely, in the Cassinian drop model, when the maximum deformation length approaches the breakup limit, the radius of the central cross-section rapidly decreases and the contour shape approaches a shape with a sharp singular point around its midpoint. Therefore, it is considered that the deformation behaviour of the proposed Cassinian droplet is very close to the deformation behaviour of a low-viscosity droplet. As mentioned in the latter part of § 3, the contour shape of an experimentally stretched low-viscosity 2-lobed droplet is very accurately approximated by the Cassinian oval curve of the optimum parameter A_{opt}, except at the moment of breakup. The inconsistency between the breakup behaviour of the Cassinian droplet and that of an actual low-viscosity droplet occurs because the surfaces of actual droplets are physically required to be smooth. Although the Cassinian function alone does not express the shape of a low-viscosity droplet at the moment of breakup, by interpolating the vicinity of the central cross-section with a hyperbolic function, it can be represented by a combination of the narrow interpolation part and the breakup limit of the Cassinian oval curve (figure 3*c*,*d*). As a low-viscosity 2-lobed droplet has a very weak restoring force owing to its viscosity, the radius of the interpolated hyperbolic region at the vicinity of its midpoint will decrease rapidly and will be broken owing to the centrifugal stress and fluid instabilities. Therefore, the maximum deformation length of low-viscosity droplets at the moment of breakup is slightly smaller than that of the Cassinian droplet at the breakup limit; $u_{*,break}$.

So far, we have demonstrated that the Cassinian droplet model is a suitable model for low-viscosity 2-lobed droplets. In the case of a high-viscosity droplet,

even though a liquid filament can form immediately before the droplet breaks up, the liquid filament can be approximated by the hyperbolic cosine interpolation function. Therefore, it is considered that the distribution of the sectional radius of the high-/moderate-viscosity droplet immediately before the breakup is represented by the combination of the elongated hyperbolic interpolation function and the Cassinian oval curve smoothly connected to the interpolation function. As mentioned in the model development section, as the stress-balance equation can be applied to a 2-lobed droplet with an arbitrary distribution of the sectional radius (equations (2.7) and (2.8)), it is expected that the breakup behaviour of high-viscosity droplets can be reproduced well by introducing an appropriate interpolation function.

Furthermore, in situations where a droplet separates from the main flow (for instance, a pinch-off process of a pendant drop consisting of low-viscosity fluid (e.g. figure 3 of Tirtaatmadja, McKinley & Cooper-White (2006), figure 4 of Clasen *et al.* (2012)) or a process of releasing bubbles from a nozzle in the water (Czerski & Deane 2010)), there is a possibility that the radius profile of the interface of axial symmetrical flow can be closely approximated by the Cassinian oval curve. From the above examples, it is considered that the outline shape of the droplet can be well approximated by the Cassinian oval curve when the axisymmetrical axis of the shape of the droplet and the direction of the driving force of the deformation are parallel. Therefore, the proposed 'Cassinian droplet model' can be applied to large deformation of droplets in such a system. In actual situations where a drop separates from high-/moderate-/low-viscosity fluid, the fluid interface has an asymmetrical complicated shape at the neck region at the moment the liquid filament breaks up (e.g. Eggers 1993; Day, Hinch & Lister 1998; Castrejón-Pita *et al.* 2015), whereas there are situations where a smooth liquid filament is observed until the moment that the drop separates (e.g. the figures in Papageorgiou 1995). In the former situations, however, the shape of the interface maintains axial symmetry and appears as a smooth liquid filament around the neck region, except for the moment when the neck collapses. It is highly possible that the radius profile of the interface of such liquid filaments can be approximated well by hyperbolic cosine interpolation function, by appropriately setting parameters of the function. Ultimately, whether the breakup of rotating moderate-/low-viscosity droplets belongs to the former or latter situations, in the process of extension and collapse of the liquid filament formed between the two lobes immediately before the droplet breaks up, the interface of the liquid filament is axially symmetrical and smooth and modelled by using the hyperbolic cosine interpolating function. Subsequently, as mentioned in this section, by modelling the shape of the interface of the stretched moderate-/low-viscosity droplet by the combination of the breakup limit of the Cassinian oval curve and an elongated hyperbolic cosine interpolation function smoothly connected to the Cassinian oval, the dimensionless deformation length is expected to be obtained as a function of the dimensionless angular velocity of rotation. Moreover, in Bhat *et al.* (2010) authors have shown beads on a string for visco-elastic fluid. Since the bead is formed only at the moment that a droplet breaks up, it seems that the liquid filament formed in the process by which a drop separates from visco-elastic fluid can be modelled in the same way. For the moment of breakup, we should also consider responses to various perturbations, as represented by Rayleigh Plateau instability. The model of rotating droplets incorporating this effect is currently under consideration.

Although there is a very slight difference between the Cassinian oval curve and the outline shape of 2-lobed droplets in rotation, the characteristic quantities obtained as functions of rotating angular velocity by using the Cassinian droplet

model approximate the deforming behaviour of actual low-viscosity droplets very well, whereas the Cassinian oval curve is a simple and easy-to-handle mathematical function with only three parameters: u_*, v_* and A. Therefore, we conclude that the Cassinian oval curve is an appropriate approximate solution of the entire shape of the interface of 2-lobed droplets and the proposed Cassinian droplet model is suitable to model the deforming behaviour of rotating 2-lobed droplets. Namely, we could have successfully proposed a quite simple but physically reliable mathematical model by setting the outline shape of the droplet to the Cassinian oval curve. As the series of Cassinian oval curves matches the contour shape of rotating 2-lobed droplets very well, the Cassinian oval function appears to have a fundamental relationship with the deformation mechanism of rotating 2-lobed droplets. By applying various extensions to the Cassinian droplet model, we can handle more complicated or unstable deformation behaviour; for example, the relaxation process in the coalescence of binary droplet collision or the formation of viscous droplets from a jet ejected from a nozzle.

Acknowledgements

We thank Satoshi Matsumoto and Yutaka Abe for providing useful experimental data for this work. This work was supported by JSPS KAKENHI grant no. 15H03925.

Appendix A. Derivation of (2.3)

In this appendix, we provide a detailed explanation of the derivation of (2.3). The Navier–Stokes (NS) equation in the rotational frame fixed to 2-lobed droplet in rotation is expressed, by repeating (2.2), as

$$\frac{\mathrm{D}\boldsymbol{u}}{\mathrm{D}t} = \frac{1}{\rho}\boldsymbol{\nabla}\cdot\tilde{\boldsymbol{\sigma}} - \boldsymbol{\omega}\times(\boldsymbol{\omega}\times\boldsymbol{r}) - 2\boldsymbol{\omega}\times\boldsymbol{u} - \left(\frac{\mathrm{D}\boldsymbol{\omega}}{\mathrm{D}t}\right)\times\boldsymbol{r}. \tag{A 1}$$

As the angular velocity vector $\boldsymbol{\omega}$ and position vector $\boldsymbol{r}$ are set as $\boldsymbol{\omega} = (0, 0, \omega)^{\mathrm{T}}$ and $\boldsymbol{r} = (x, y, z)^{\mathrm{T}} = (x, r\cos\theta, r\sin\theta)^{\mathrm{T}}$, respectively, the term of centrifugal force in (A 1) is calculated as follows:

$$\begin{aligned} -\boldsymbol{\omega}\times(\boldsymbol{\omega}\times\boldsymbol{r}) &= -(0, 0, \omega)^{\mathrm{T}}\times((0, 0, \omega)^{\mathrm{T}}\times(x, y, z)^{\mathrm{T}}) \\ &= -(0, 0, \omega)^{\mathrm{T}}\times(-y\omega, x\omega, 0)^{\mathrm{T}} \\ &= (x\omega^2, y\omega^2, 0)^{\mathrm{T}} \\ &= \boldsymbol{\nabla}\left(\tfrac{1}{2}(x^2+y^2)\omega^2\right). \end{aligned} \tag{A 2}$$

Substituting above, the NS equation is rewritten as

$$\frac{\mathrm{D}\boldsymbol{u}}{\mathrm{D}t} = \frac{1}{\rho}\boldsymbol{\nabla}\cdot\tilde{\boldsymbol{\sigma}} + \boldsymbol{\nabla}\left(\frac{1}{2}(x^2+y^2)\omega^2\right) + \begin{pmatrix} 2\omega u_y + \dot{\omega}y \\ -2\omega u_x - \dot{\omega}x \\ 0 \end{pmatrix}. \tag{A 3}$$

In order to obtain the stress-balance equation in the longitudinal direction of the rotating 2-lobed droplet and the equation of angular momentum, we classify the terms of (A 3) by the direction of integration over the cross-section of the droplet at the position x, $y^2 + z^2 \leqslant h(x)^2$. The integral of the inertial force, the integral of internal stress and the integral of centrifugal force are along the x-direction owing to the symmetry of the integral region. Considering the term of Coriolis force and the

Euler force, the x-component of the integration of the last term of (A 3) within the cross-section of the droplet at the position x is calculated as

$$\int_0^{h(x)} \int_0^{2\pi} (2\omega(\dot{r}\cos\theta - r\dot{\theta}\sin\theta) + \dot{\omega} r\cos\theta) r \,\mathrm{d}r\,\mathrm{d}\theta = \int_0^{h(x)} \left(\int_0^{2\pi} (2\omega u_r \cos\theta + \dot{\omega} r\cos\theta)\,\mathrm{d}\theta \right) r\,\mathrm{d}r = 0. \tag{A 4}$$

In the above calculation, $u_\theta = r\dot{\theta} = 0$ because the internal flow of the droplet is axisymmetric with respect to x-axis. Therefore, the resultant force of Coriolis force and Euler force on the cross-section at the position x is along the y-direction. Thus, the stress-balance equation in the direction of $\boldsymbol{e}_x$ is expressed as

$$\int_{V/2} \frac{\mathrm{D}^2 \boldsymbol{r}}{\mathrm{D}t^2}\,\mathrm{d}V = \int_{V/2} \frac{1}{\rho} \boldsymbol{\nabla}\cdot\tilde{\boldsymbol{\sigma}}\,\mathrm{d}V + \int_{V/2} \boldsymbol{\nabla}\left(\frac{1}{2}(x^2+y^2)\omega^2\right)\,\mathrm{d}V, \tag{A 5}$$

where the region of integration $V/2$ is the right half of the droplet, which is expressed as $y^2 + z^2 \leqslant h(x)^2 (0 \leqslant x \leqslant R_{Max})$. By applying the generalised Stokes' theorem, we obtain

$$\int_{V/2} \boldsymbol{\nabla}\cdot\tilde{\boldsymbol{\sigma}}\,\mathrm{d}V = \int_{\partial(V/2)} \tilde{\boldsymbol{\sigma}}\cdot\boldsymbol{n}\,\mathrm{d}S \tag{A 6}$$

and

$$\int_{V/2} \boldsymbol{\nabla}\left(\frac{1}{2}(x^2+y^2)\omega^2\right)\mathrm{d}V = \int_{\partial(V/2)} \left(\frac{1}{2}(x^2+y^2)\omega^2\right)\boldsymbol{n}\,\mathrm{d}S, \tag{A 7}$$

and by using the boundary condition, $\tilde{\boldsymbol{\sigma}}\cdot\boldsymbol{n} = -\gamma\kappa\boldsymbol{n}$ on the free surface of the droplet, we obtain the integral form of the stress-balance equation in the direction of $\boldsymbol{e}_x$ as follows:

$$\rho \int_{V/2} \frac{\mathrm{D}^2}{\mathrm{D}t^2}\boldsymbol{r} r\,\mathrm{d}r\,\mathrm{d}\theta\,\mathrm{d}x = \int_{C_0} \tilde{\boldsymbol{\sigma}}\cdot\boldsymbol{n}\,\mathrm{d}S - \gamma\int_{S_f} \boldsymbol{n}\kappa\,\mathrm{d}S + \rho\int_{C_0} \boldsymbol{n}\frac{1}{2}\omega^2(x^2+y^2)\,\mathrm{d}S + \rho\int_{S_f} \boldsymbol{n}\frac{1}{2}\omega^2(x^2+y^2)\,\mathrm{d}S. \tag{A 8}$$

The above equation is the same as (2.3).

Appendix B. Supplementary explanations about Cassinian oval curves

In this section, we provide supplementary explanations about the Cassinian oval curves. In the proposed model of a 2-lobed droplet, the outline shape of the droplet is represented by using the Cassinian oval curve

$$F(x_*, z_*) = (Ax_*^2 + z_*^2)^2 - (Au_*^2 - v_*^2)(Ax_*^2 - z_*^2) - Au_*^2 v_*^2 = 0 \quad (Au_* > v_* > 0). \tag{B 1}$$

As mentioned in the main text, the shape of a Cassinian oval curve depends, up to mathematical similarity, on $k = u_*/v_*$ and the parameter A. This is proved as follows. By dividing (B 1) by u_*^4, we obtain

$$\left(A\left(\frac{x_*}{u_*}\right)^2 + \left(\frac{z_*}{u_*}\right)^2\right)^2 - \left(A - \left(\frac{v_*}{u_*}\right)^2\right)\left(A\left(\frac{x_*}{u_*}\right)^2 - \left(\frac{z_*}{u_*}\right)^2\right) - A\left(\frac{v_*}{u_*}\right)^2 = 0. \tag{B 2}$$

By substituting $k = u_*/v_*$ and introducing new variables $X_* = x_*/u_*$ and $Z_* = z_*/u_*$, we obtain

$$\left(AX_*^2 + Z_*^2\right)^2 - \left(A - \frac{1}{k^2}\right)\left(AX_*^2 - Z_*^2\right) - \frac{A}{k^2} = 0. \tag{B 3}$$

The curve defined by (B 2) and the curve defined by (B 3) are mathematically similar to each other and the ratio of similitude between the two curves is u_*. Thus, if the values of the two dimensionless parameters $k = u_*/v_*$ and A are set, the shape of the Cassinian droplet itself is determined. The ratio of similitude, u_*, is calculated from the volume conservation equation (3.1) for each set of values of k and A.

We demonstrate that a Cassinian oval curve can assume the shape of a 2-lobed closed curve. By calculating the first-order and second-order derivatives of $F(x_*, z_*)$ represented in (B 1), we obtain

$$\frac{\partial F}{\partial x_*} + \left(\frac{\partial F}{\partial z_*}\right)\left(\frac{\mathrm{d}z_*}{\mathrm{d}x_*}\right) = 0 \Leftrightarrow \left(\frac{\mathrm{d}z_*}{\mathrm{d}x_*}\right) = -\frac{Ax_*(-Au_*^2 + v_*^2 + 2Ax_*^2 + 2z_*^2)}{z_*(-v_*^2 + Au_*^2 + 2Ax_*^2 + 2z_*^2)}, \tag{B 4}$$

$$\frac{\partial^2 F}{\partial x_*^2} + 2\left(\frac{\partial^2 F}{\partial x_* \partial z_*}\right)\left(\frac{\mathrm{d}z_*}{\mathrm{d}x_*}\right) + \left(\frac{\partial^2 F}{\partial z_*^2}\right)\left(\frac{\mathrm{d}z_*}{\mathrm{d}x_*}\right)^2 + \left(\frac{\partial F}{\partial z_*}\right)\left(\frac{\mathrm{d}^2 z_*}{\mathrm{d}x_*^2}\right) = 0. \tag{B 5}$$

By solving the equation $(\mathrm{d}z_*/\mathrm{d}x_*) = 0$ and (B 1), it can be shown that $(\mathrm{d}z_*/\mathrm{d}x_*)$ becomes 0 at

$$x_* = 0, \pm\sqrt{\frac{(Au_*^2 - 3v_*^2)(3Au_*^2 - v_*^2)}{8A(Au_*^2 - v_*^2)}} \tag{B 6}$$

if $Au_*^2 - 3v_*^2 > 0$, that is, $k^2 - 3/A > 0$. Further, it is possible to investigate whether the curve is convex in the vicinity of a certain point (x_*, z_*) by using (B 5). By applying the formula to (2.9), the second-order derivative of z_* at the vicinity of $(0, v_*)$ is calculated as

$$\frac{\mathrm{d}^2 z_*}{\mathrm{d}x_*^2} = \frac{A(Au_*^2 - 3v_*^2)}{v_*(Au_*^2 + v_*^2)} > 0 \quad (Au_*^2 - 3v_*^2 > 0). \tag{B 7}$$

Therefore, when $Au_*^2 - 3v_*^2 > 0$, i.e. $k^2 - 3/A > 0$, the Cassinian oval curve is concave at the vicinity of the point $(0, v_*)$. By using these and the fact that $|\mathrm{d}z_*/\mathrm{d}x_*| \to \infty$ as $x_* \to \pm u_*$ (refer to figure 1), it can be shown that the upper branch of the Cassinian oval curve has two local maximum points and one local minimum point. Since the lower branch of the Cassinian oval curve is symmetrical to the upper branch with respect to the x_*-axis, the entire shape of the Cassinian oval curve is 2-lobed when $Au_*^2 - 3v_*^2 > 0 \Leftrightarrow k^2 - 3/A > 0$.

Appendix C. Detailed expressions of equations appearing in § 3

In this section, we describe the equations derived in the process of drawing the plot of $u_*(k; A)$ versus $\omega_{*,s}(k; A)$ and obtaining the condition of linear stability (equation (3.10)).

In the proposed model of a 2-lobed droplet, the radius of the cross-section at the position x_* is expressed, by repeating (2.10), as

$$h_*(x_*) = \sqrt{\tfrac{1}{2}\left(-Au_*^2 + v_*^2 - 2Ax_*^2 + \sqrt{(Au_*^2 + v_*^2)^2 + 8A(Au_*^2 - v_*^2)x_*^2}\right)}. \tag{C 1}$$

By applying integral formulas

$$\int \sqrt{x^2+a^2}\,\mathrm{d}x = \frac{1}{2}(x\sqrt{x^2+a^2} + a^2\log_e[x+\sqrt{x^2+a^2}]) + C, \tag{C 2}$$

$$\int x^2\sqrt{x^2+a^2}\,\mathrm{d}x = \frac{1}{8}(x(2x^2+a^2)\sqrt{x^2+a^2} - a^4\log_e[x+\sqrt{x^2+a^2}]) + C, \tag{C 3}$$

the dimensionless volume of the right half of the droplet ($0 \leqslant x \leqslant R_{Max},\ \ 0 \leqslant \theta \leqslant 2\pi$) is explicitly calculated as expressed in (3.1). Substituting u_*/k for v_* and solving the equation for u_*, the dimensionless deformation length u_* can be written as a single-variable function of k with a parameter A such that

$$u_*(k;A) = \left[\frac{32Ak^3(Ak^2-1)}{-4kA(3-4k^2A+k^4A^2) + 3\sqrt{2}\sqrt{A(-1+k^2A)}(1+k^2A)^2\log_e\left(\dfrac{-1+3k^2A+2\sqrt{2}k\sqrt{A(-1+k^2A)}}{1+k^2A}\right)}\right]^{1/3}. \tag{C 4}$$

The dimensionless radius of the central cross-section v_* is expressed as

$$v_*(k;A) = \left[\frac{32A(Ak^2-1)}{-4kA(3-4k^2A+k^4A^2) + 3\sqrt{2}\sqrt{A(-1+k^2A)}(1+k^2A)^2\log_e\left(\dfrac{-1+3k^2A+2\sqrt{2}k\sqrt{A(-1+k^2A)}}{1+k^2A}\right)}\right]^{1/3}. \tag{C 5}$$

Further, $u_*(k;A)$ and $v_*(k;A)$ are continuous monotonic functions of k with a single parameter A. As $k \to \infty$, even though $v_*(k;A)$ converges to 0, $u_*(k;A)$ approaches the finite value $u_{*,break}$, which is defined as

$$u_{*,break} = \frac{4}{(6\sqrt{2}\log_e(3+2\sqrt{2}) - 8)^{1/3}} \cdot A^{-1/3} \simeq 2.095A^{-1/3}. \tag{C 6}$$

When (C 4) and (C 5) are substituted into (3.2)–(3.4), each term of these equations is also expressed as a single-variable function of k with the parameter A. The full expression of $x_{g*}(k;A)$ as a function of k can be written as

$$\begin{aligned} x_{g*}(k;A) \;=\; & 2^{20/3}\cdot\frac{1+4k^2A+k^4A^2}{3k^4A}\left[\frac{1}{k^3A(-1+k^2A)}\left(-4kA(3-4k^2A+k^4A^2)\right.\right. \\ & +3\sqrt{2}\sqrt{A(-1+k^2A)}(1+k^2A)^2 \\ & \left.\left.\times\log_e\left(\frac{-1+3k^2A+2\sqrt{2}k\sqrt{A(-1+k^2A)}}{1+k^2A}\right)\right)\right]^{-4/3}, \end{aligned} \tag{C 7}$$

and $K(k;A)$, which is a term relating to twice the mean curvature of the midpoint, is expressed as

$$\begin{aligned} K(k;A) \;=\; & 2^{5/3}\cdot\frac{1-3A+A(A+1)k^2}{k+k^3A}\left[\frac{1}{k^3A(-1+k^2A)}\left(-4kA(3-4k^2A+k^4A^2)\right.\right. \\ & +3\sqrt{2}\sqrt{A(-1+k^2A)}(1+k^2A)^2 \\ & \left.\left.\times\log_e\left(\frac{-1+3k^2A+2\sqrt{2}k\sqrt{A(-1+k^2A)}}{1+k^2A}\right)\right)\right]^{-1/3}. \end{aligned} \tag{C 8}$$

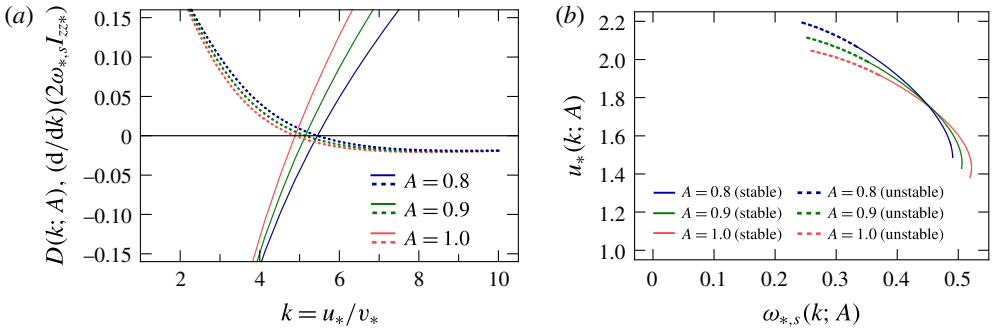

FIGURE 6. (Colour online) Calculation results derived from the proposed model are plotted for different values of the parameter A. Red lines, green lines and blue lines correspond to the plots for $A = 1.0$, $A = 0.9$, $A = 0.8$, respectively. (*a*) $D(k;A)$ and $(\mathrm{d}/\mathrm{d}k)(2\omega_{*,s}(k;A)I_{zz*}(k;A))$ are plotted as functions of k. For each value of A, $D(k;A)$ and $(\mathrm{d}/\mathrm{d}k)(2\omega_{*,s}I_{zz*})$ are monotonic functions that intercept the horizontal line at $k = k_{crit,A}$. (*b*) Parametric plots of $(\omega_{*,s}(k;A), u_*(k;A))$ are illustrated for $A = 1.0$, 0.9 and 0.8. Each solid line is a set of linearly stable solutions and each broken line is the set of unstable solutions for the corresponding value of A.

Therefore, the stationary solution of ω_* is provided for arbitrary values of k and A such that

$$\omega_{*,s}(k;A) = \frac{1}{4}\left[\frac{3(1-3A+A(1+A)k^2)}{-2-8k^2A+8k^6A^3+2k^8A^4}\left(-4kA(3-4k^2A+k^4A^2)\right.\right.$$
$$+3\sqrt{2}\sqrt{A(-1+k^2A)}(1+k^2A)^2$$
$$\left.\left.\times\log_e\left(\frac{-1+3k^2A+2\sqrt{2}k\sqrt{A(-1+k^2A)}}{1+k^2A}\right)\right)\right]^{1/2}. \tag{C 9}$$

In figure 6, a parametric plot of $(\omega_{*,s}(k;A), u_*(k;A))$ is illustrated for several values of A.

Reapplying the integral formulas, the dimensionless moment of inertia of the right half of the droplet $(0 \leqslant x \leqslant R_{Max},\ \ 0 \leqslant \theta \leqslant 2\pi)$ is explicitly calculated as

$$I_{zz*} = \frac{1}{30720}\left(8A(-118+267A)u_*^5+640(2+3A)u_*^3v_*^2+\frac{120(2+15A)u_*v_*^4}{A}\right.$$
$$-960\frac{(-2+A)A^2u_*^7}{Au_*^2-v_*^2}+\frac{30\sqrt{2A(Au_*^2-v_*^2)}}{A^2(Au_*^2-v_*^2)^2}$$
$$\times(Au_*^2+v_*^2)^2\left(A^2(2+15A)u_*^4+2(2-17A)Au_*^2v_*^2+(2+15A)v_*^4\right)$$
$$\left.\times\log_e\left[\frac{Au_*^2+v_*^2}{2\sqrt{2}u_*\sqrt{A(Au_*^2-v_*^2)}+3Au_*^2-v_*^2}\right]\right). \tag{C 10}$$

Substituting (C 4)–(C 5) into (C 10), the dimensionless moment of inertia of the right half of the droplet, $I_{zz*}(k;A)$, is also expressed as a single-variable function of k with the parameter A.

We now demonstrate a detailed expression of the (3,1) component of the Jacobian matrix (3.8). Linearising (3.4) around $(k, \omega_*, \ell) = (k, \omega_{*,s}, 0)$, we obtain

$$\begin{aligned} J_{31} &= \frac{\partial}{\partial k}\left(-\frac{x''_{g*}(k;A)}{x'_{g*}(k;A)}\ell^2 + \frac{x_{g*}(k;A)}{x'_{g*}(k;A)}\omega_*^2 - \frac{K(k;A)}{x'_{g*}(k;A)}\right. \\ &\quad \left. + N\cdot\frac{v_*(k;A)v'_*(k;A)}{x'_{g*}(k;A)}\ell\right)\Bigg|_{\substack{\omega_*=\omega_{*,s}(k;A)\\ \ell=0}} \\ &= \left(\left(-\frac{x''_{g*}(k;A)}{x'_{g*}(k;A)}\right)'\ell^2 + \left(\frac{x_{g*}(k;A)}{x'_{g*}(k;A)}\right)'\omega_*^2 - \left(\frac{K(k;A)}{x'_{g*}(k;A)}\right)'\right. \\ &\quad \left. + N\cdot\left(\frac{v_*(k;A)v'_*(k;A)}{x'_{g*}(k;A)}\right)'\ell\right)\Bigg|_{\substack{\omega_*=\omega_{*,s}(k;A)\\ \ell=0}} \\ &= \omega_{*,s}^2(k;A)\left(1 - \frac{x_{g*}(k;A)x''_{g*}(k;A)}{x'^2_{g*}(k;A)}\right) + \frac{K(k;A)x''_{g*}(k;A)}{x'^2_{g*}(k;A)} - \frac{K'(k;A)}{x'_{g*}(k;A)}. \end{aligned} \tag{C 11}$$

According to this equation, $D(k;A)$, which is defined in (3.10), can be expressed as

$$\begin{aligned} D(k;A) &= \omega_{*,s}^2(k;A)\left(1 - \frac{x_{g*}(k;A)x''_{g*}(k;A)}{x'^2_{g*}(k;A)} - 2\frac{I'_{zz*}(k;A)x_{g*}(k;A)}{I_{zz*}(k;A)x'_{g*}(k;A)}\right) \\ &\quad + \frac{K(k;A)x''_{g*}(k;A)}{x'^2_{g*}(k;A)} - \frac{K'(k;A)}{x'_{g*}(k;A)}. \end{aligned} \tag{C 12}$$

$D(k;A)$ is a monotonically increasing function of k that crosses the line $D = 0$ at $k = k_{crit,A}$, and the angular momentum of the Cassinian drop changes from an increasing trend to a decreasing trend at the same point $k_{crit,A}$ (figure 6*a*). Therefore, the stationary solution of $u_* < u_{*crit,A}$ (the solid lines in figure 6*b*) can be reproduced by quasi-statically adding angular momentum in the laboratory.

REFERENCES

AUSSILLOUS, P. & QUÉRÉ, D. 2004 Shapes of rolling liquid drops. *J. Fluid Mech.* **512**, 133–151.

BALDWIN, K. A., BUTLER, S. L. & HILL, R. J. A. 2015 Artificial tektites: an experimental technique for capturing the shapes of spinning drops. *Sci. Rep.* **5**, 7660.

BASSET, A. B. 1901 *An Elementary Treatise on Cubic and Quartic Curves*. Deighton, Bell.

BEAUGNON, E., FABREGUE, D., BILLY, D., NAPPA, J. & TOURNIER, R. 2001 Dynamics of magnetically levitated droplets. *Physica* B **294**, 715–720.

BEAUGNON, E. & TOURNIER, R. 1991 Levitation of water and organic substances in high static magnetic fields. *J. Phys.* III **1** (8), 1423–1428.

BENNER, R. E., BASARAN, O. A. & SCRIVEN, L. E. 1991 Equilibria, stability and bifurcations of rotating columns of fluid subjected to planar disturbances. *Proc. R. Soc. Lond.* A **433** (1887), 81–99.

BHAT, P. P., APPATHURAI, S., HARRIS, M. T., PASQUALI, M., MCKINLEY, G. H. & BASARAN, O. A. 2010 Formation of beads-on-a-string structures during break-up of viscoelastic filaments. *Nat. Phys.* **6** (8), 625–631.

VAN DER BOS, A., VAN DER MEULEN, M.-J., DRIESSEN, T., VAN DEN BERG, M., REINTEN, H., WIJSHOFF, H., VERSLUIS, M. & LOHSE, D. 2014 Velocity profile inside piezoacoustic inkjet droplets in flight: comparison between experiment and numerical simulation. *Phys. Rev. Appl.* **1** (1), 014004.

BRANDT, E. H. 1989 Levitation in physics. *Science* **243** (4889), 349–355.

BROWN, R. A. & SCRIVEN, L. E. 1980 The shape and stability of rotating liquid drops. *Proc. R. Soc. Lond.* A **371** (1746), 331–357.

BUTLER, S. L., STAUFFER, M. R., SINHA, G., LILLY, A. & SPITERI, R. J. 2011 The shape distribution of splash-form tektites predicted by numerical simulations of rotating fluid drops. *J. Fluid Mech.* **667**, 358–368.

CASTREJÓN-PITA, J. R., CASTREJÓN-PITA, A. A., THETE, S. S., SAMBATH, K., HUTCHINGS, I. M., HINCH, J., LISTER, J. R. & BASARAN, O. A. 2015 Plethora of transitions during breakup of liquid filaments. *Proc. Natl Acad. Sci.* **112** (15), 4582–4587.

CHANDRASEKHAR, S. 1965 The stability of a rotating liquid drop. *Proc. R. Soc. Lond.* A **286** (1404), 1–26.

CHANDRASEKHAR, S. 1967 Ellipsoidal figures of equilibrium–an historical account. *Commun. Pure Appl. Maths* **20** (2), 251–265.

CLASEN, C., PHILLIPS, P. M., PALANGETIC, L. & VERMANT, J. 2012 Dispensing of rheologically complex fluids: the map of misery. *AIChE J.* **58** (10), 3242–3255.

CZERSKI, H. & DEANE, G. B. 2010 Contributions to the acoustic excitation of bubbles released from a nozzle. *J. Acoust. Soc. Am.* **128** (5), 2625–2634.

DAY, R. F., HINCH, E. J. & LISTER, J. R. 1998 Self-similar capillary pinchoff of an inviscid fluid. *Phys. Rev. Lett.* **80** (4), 704–707.

EGGERS, J. 1993 Universal pinching of 3d axisymmetric free-surface flow. *Phys. Rev. Lett.* **71** (21), 3458–3460.

EGGERS, J. 1997 Nonlinear dynamics and breakup of free-surface flows. *Rev. Mod. Phys.* **69**, 865–930.

EGGERS, J. & DUPONT, T. F. 1994 Drop formation in a one-dimensional approximation of the navier–stokes equation. *J. Fluid Mech.* **262**, 205–221.

EGGERS, J. & FONTELOS, M. A. 2005 Isolated inertialess drops cannot break up. *J. Fluid Mech.* **530**, 177–180.

ELKINS-TANTON, L. T., AUSSILLOUS, P., BICO, J., QUERE, D. & BUSH, J. W. M. 2003 A laboratory model of splash-form tektites. *Meteorit. Planet. Sci.* **38** (9), 1331–1340.

FORESTI, D., NABAVI, M., KLINGAUF, M., FERRARI, A. & POULIKAKOS, D. 2013 Acoustophoretic contactless transport and handling of matter in air. *Proc. Natl Acad. Sci. USA* **110** (31), 12549–12554.

FROHN, A. & ROTH, N. 2000 *Dynamics of Droplets*. Springer.

HEINE, C.-J. 2006 Computations of form and stability of rotating drops with finite elements. *IMA J. Numer. Anal.* **26** (4), 723–751.

HILL, R. J. A. & EAVES, L. 2008 Nonaxisymmetric shapes of a magnetically levitated and spinning water droplet. *Phys. Rev. Lett.* **101**, 234501.

LANDAU, L. D. & LIFSHITS, E. M. 1959 *Fluid Mechanics*. Pergamon Press.

OHSAKA, K., REDNIKOV, A., SADHAL, S. S. & TRINH, E. H. 2002 Noncontact technique for determining viscosity from the shape relaxation of ultrasonically levitated and initially elongated drops. *Rev. Sci. Instrum.* **73** (5), 2091–2096.

PAPAGEORGIOU, D. T. 1995 On the breakup of viscous liquid threads. *Phys. Fluids* **7** (7), 1529–1544.

PATZEK, T. W., BASARAN, O. A., BENNER, R. E. & SCRIVEN, L. E. 1995 Nonlinear oscillations of two-dimensional, rotating inviscid drops. *J. Comput. Phys.* **116** (1), 3–25.

POINCARÉ, H. 1885 Sur l'équilibre d'une masse fluide animée d'un mouvement de rotation. *Acta Mathematica* **7** (1), 259–380.

QIAN, J. & LAW, C. K. 1997 Regimes of coalescence and separation in droplet collision. *J. Fluid Mech.* **331**, 59–80.

RAYLEIGH, LORD 1879 On the capillary phenomena of jets. *Proc. R. Soc. Lond.* **29** (196–199), 71–97.

RHIM, W.-K., CHUNG, S. K. & ELLEMAN, D. D. 1990 Experiments on rotating charged liquid drops. *AIP Conf. Proc.* **197** (1), 91–105.

RHIM, W.-K., COLLENDER, M., HYSON, M. T., SIMMS, W. T. & ELLEMAN, D. D. 1985 Development of an electrostatic positioner for space material processing. *Rev. Sci. Instrum.* **56** (2), 307–317.

SUN, K., ZHANG, P., LAW, C. K. & WANG, T. 2015 Collision dynamics and internal mixing of droplets of non-newtonian liquids. *Phys. Rev. Appl.* **4** (5), 054013.

TANAKA, R., MATSUMOTO, S., KANEKO, A. & ABE, Y. 2013 Viscosity measurement using breakup of a levitated droplet by rotation. *Interfacial Phenom. Heat Transfer* **1** (2), 181–194.

TIRTAATMADJA, V., MCKINLEY, G. H. & COOPER-WHITE, J. J. 2006 Drop formation and breakup of low viscosity elastic fluids: effects of molecular weight and concentration. *Phys. Fluids* **18** (4), 043101.

TRINH, E. H. 1985 Compact acoustic levitation device for studies in fluid dynamics and material science in the laboratory and microgravity. *Rev. Sci. Instrum.* **56** (11), 2059–2065.

WANG, T. G., ANILKUMAR, A. V., LEE, C. P. & LIN, K. C. 1994 Bifurcation of rotating liquid drops: results from usml-1 experiments in space. *J. Fluid Mech.* **276**, 389–403.

WANG, T. G., TRINH, E. H., CROONQUIST, A. P. & ELLEMAN, D. D. 1986 Shapes of rotating free drops: spacelab experimental results. *Phys. Rev. Lett.* **56**, 452–455.